

Defocusing μ PTV with increased measurement depth using shadowgraphy

T. Fuchs* , C. Burkhardt, C. J. Kähler 

Universität der Bundeswehr München
Institute of Fluid Mechanics and Aerodynamics
85577 Neubiberg, Germany

*Corresponding author: thomas.fuchs@unibw.de

Keywords: defocusing PTV, astigmatism PTV, microfluidics, shadowgraphy

ABSTRACT

In this study we can show that shadowgraphy is a feasible alternative to fluorescence for microscopic particle imaging. Furthermore, using the particle shadow image geometry (diameter for defocusing methods or axis lengths for astigmatism methods), the particle location along the optical axis can be determined, enabling a three-dimensional flow velocity measurement with a single camera. However, the rate of change of the particle shadow image geometry as a function of the distance to the focal plane is one order of magnitude smaller as compared to fluorescence/scattering imaging approaches, such that the measurement depths is effectively increased. This increase is due to the fact that the signal to noise ratio of the relatively small particle shadow images is large, even if the particle is located far away from the focal plane, as the intensity is distributed over a small sensor area. In addition, due to their smaller dimensions, more particle shadow images can be captured on the camera sensor, yielding a larger information density for microscopic particle imaging. A measurement of a micro-channel (channel height: 650 μm) flow showed a good agreement with the ideal parabolic flow profile, proving the viability of this microscopic particle shadow imaging approach as a suitable addition to the existing fluorescence-based methods.

1. Introduction

Using the out of focus information of particle images is a standard practice in microfluidics to determine the spatial particle location, as outlined in the topical review of Cierpka & Kähler (2012). The defocusing principle was first proposed by Willert & Gharib (1992) in a macroscopic set-up. Astigmatism as a means to break the symmetry of the optical configuration, initially applied by Kao & Verkman (1994), provides a more homogeneous distribution of the signal to noise ratio of the particle imaged at different off focus locations along the optical axis. However, defocusing imaging results in a linear relation between the particle image diameter and the particle z location at a sufficient distance from the focal plane (Olsen & Adrian (2000) and Rossi & Kähler (2014)). This linearity allows for deriving the defocusing function from measured data for macroscopic as

well as for microscopic experiments, as shown by Fuchs et al. (2016) and Leister et al. (2021), respectively. For confined geometries, where it is impossible to perform a scanning calibration which is required for some defocusing algorithms (e.g. Barnkob et al. (2015)), an *in situ* calibration is an inevitable feature.

Particle imaging in micro channels, or generally in microscopic environments, is most often performed with the help of fluorescent seeding particles. The particles emit light at a larger wavelength than the excitation light wave length, which can then be filtered out. As a result, only the particles are imaged and background reflections from surfaces are suppressed. However, fluorescent labelling is associated with the use of surfactants, changing the interfacial tensions (Thijssen et al., 2011). Thus, for applications, where for instance, the surface tension or contact angles, are a sensitive quantity, the use of fluorescent particles is a drawback.

In this study, we assess a microscopic defocusing imaging system which is based on shadowgraphy, which therefore does not rely on fluorescent particles. Moreover, as compared with fluorescent or scattered light, the defocusing function of the imaged particles is less steep, meaning that the particle image diameter increases at a low rate with distance to the focal plane. As a consequence, the measurement depth is increased. Additionally introducing astigmatism to the imaging optics results in an extent of the measurement domain that is similar for the 3 spatial directions, while at the same time a relatively large particle image concentration can be achieved.

2. Defocusing shadowgraphy

Experimental set-up

In particle shadowgraph imaging, the shadows of the particles are recorded on camera sensors. Just like in standard defocusing imaging that is based on particle scattering or fluorescent particles, the particle location along the optical axis can be deduced from the particle shadow image geometry, i.e. the image diameter. Figure 1 is showing a schematic of the defocusing μ PTV shadowgraphy set-up. For the back-light illumination, a white-light light-emitting diode (LED) was used, where the optics ensured that the illumination was only slightly divergent ($\approx 5^\circ$). The optics were positioned at a distance of around 50 mm away from the measurement domain, comprising commercially available *ibidi* micro channels. The channel flow was captured using a *PCO dimax HS4* high-speed camera (sensor: 2000×2000 pixel; pixel size: $11 \mu\text{m}$) operating with an exposure time ranging between $10\text{--}30 \mu\text{s}$, equipped with a *Zeiss M5X/0.16 420330-9901* microscope objective lens. This optical configuration yielded a reproduction scale of $s^{XY} \approx 1.8 \mu\text{m}/\text{pixel}$ and a magnification of $M \approx 6.2$. The initial experiments presented here were conducted using monodisperse polystyrene particles from *micro particles GmbH* with an average diameter of $10.07 \mu\text{m}$.

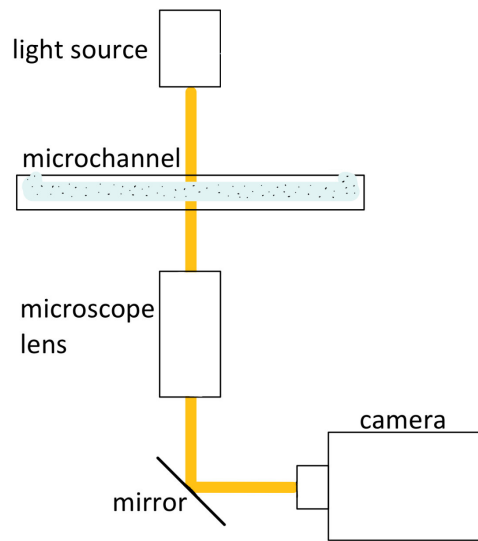


Figure 1. Schematic of the experimental set-up for microscopic defocusing PTV using white-light background illumination with a parallel light beam for shadowgraph imaging.

Particle shadow image characteristics

Unlike standard particle images, the particle shadow images show an intensity distribution which drops below the image background intensity. In fact, the closer the particle is located to the focal plane, the larger is the intensity (I) drop, as illustrated in Fig. 2 for particle shadow images, derived from the very same particle, at different distances, Δz_f , from the focal plane along the optical axis. Furthermore, a slight intensity increase can be observed in the particle image center, around $X_{\text{rel}} = 0$, while the local maximum is still well below the background intensity. As it is the case for standard defocused particle images, an outer ring, with higher intensity than the background, forms. The intensity of this outer ring first increases with distance from the focal plane, while it starts to decay after reaching a maximum. Altogether, the signal to noise ratio of the particle image decreases with Δz_f , since the intensity drop as well as the maximum of the outer ring becomes smaller relative to the background intensity.

Image processing

The approach to detect the particle shadow images is somewhat different than compared to standard particle images; the procedure for the standard images is described in detail in Fuchs et al. (2016). Prior to the particle shadow image geometry determination, following pre-processing steps of the recordings were performed: (1) An image intensity normalization with respect to the first recording; compensation for illumination intensity fluctuations. (2) A subtraction of an average image of all recordings from each recording; removal of stationary background reflections. (3) A subtraction of the sliding minimum intensity over a 20 pixel kernel for each recording individually;

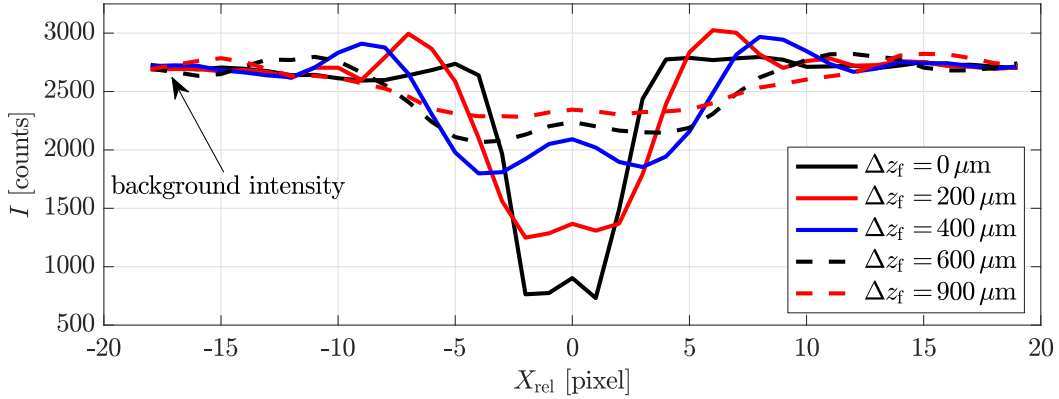


Figure 2. Line plot of the image intensity through the particle shadow image center along the sensor X coordinate for a particle imaged at different distances, Δz_f , from the focal plane. The intensity drops below the background intensity in the center part of the particle shadow image, while it features an outer ring with an intensity that is larger than that of the background.

compensation of local intensity fluctuations. (4) Intensity inversion ($I_{\text{inv}} = 0$) of each recording; detectability of the shadows. These pre-processing steps are required to identify the image locations where the intensity is lower than background intensity. After the intensity inversion, these low intensity locations are the ones with highest intensity, denoting the locations of the particle image shadows.

Following the pre-processing and the detection of the shadows, the diameter of the particle shadow images is determined. To do so, the local intensity distributions at the 4 vertices – the extrema of the outer ring in sensor X and Y direction – of the circular shadow image are analyzed. The intensities, reaching from the center of the particle image to beyond the maximum of the outer ring, are fitted by means of a thin-plate spline fit. At each vertex, the edge location of the shadow image is set to be where the local intensity lies at a threshold of 0.8 between the maximum and minimum intensity of the fit region. This edge location determination paradigm is illustrated in Fig. 3. The particle shadow image diameter, A_{XY} , is then the average of the particle extent, A , in sensor X and Y direction:

$$A_{XY} = \frac{A_X + A_Y}{2}, \quad (1)$$

whereas the center of the shadow image lies halfway between the 4 determined edge locations. The search direction for the edge location is facing outward from the particle image center at $X_{\text{loc}} = 0$, towards the outer ring. Thus, the edge location of the particle shadow image is situated closer to the image center than the outer ring, since the intensity gradient and the signal to noise ratio is the largest in that region. For standard particle images this not the case; there, the strongest intensity gradient can be found at the outer ring, but on the side further away from the image center. In the following, the defocusing characteristics of the shadowgraphy set-up are analyzed in more detail.

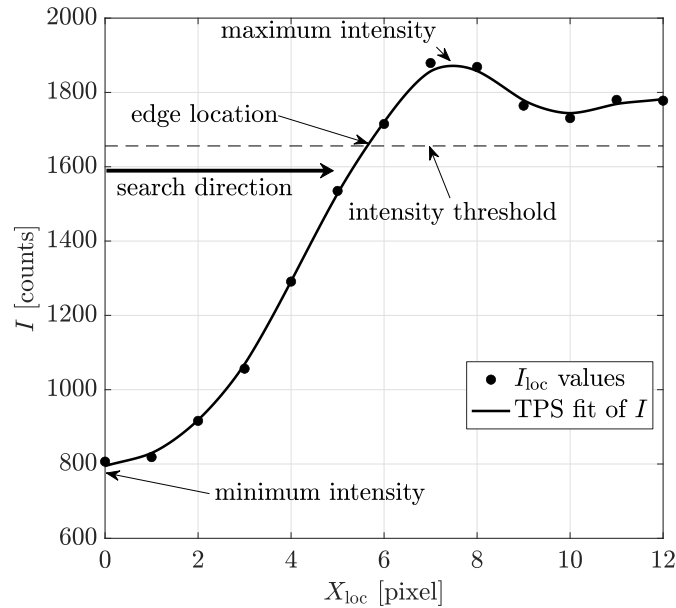


Figure 3. Illustration of the particle shadow image edge location determination: The edge is set to be where the local intensity distribution reaches 0.8 of the value between the minimum and the maximum intensity value. Thus, local intensity variations are accounted for.

Defocusing characteristics

In principle, the slope of the defocusing function determines how accurate the particle location along the optical axis, z , can be determined. If the particle image diameter increases at a high rate with distance to the focal plane, the z location can be determined more accurately. However, with increasing diameter the signal to noise ratio (SNR) of the particle image decreases, since the emitted light is distributed over a larger sensor area. Moreover, the number of particle image overlaps increases, due to their size, limiting the particle image concentration and increasing the measurement uncertainty. Effectively, the measurement depth is limited due to these two aforementioned effects.

Olsen & Adrian (2000) presented a formula for the defocusing function in microscopic optical systems using scattered light and fluorescence, which provides an estimate of the particle image diameter over z relation as a function of the optical parameters. For the optics used in this experiment ($M \approx 6.2$), the slope of the function calculated from Olsen & Adrian (2000) formula yields a value of $s^Z \approx 1.54$, meaning that over a certain z distance along the optical axis (unit: [μm]), the particle image diameter (unit: [μm]) increases by a factor of 1.54. Practically, using the background illumination, the experimentally determined slope of the defocusing function strongly deviates from this theoretical value. As plotted in Fig. 4, the slope of the defocusing function yields only around $s^Z \approx 0.18$, which denotes a particle image diameter change rate that is almost 6 times less than compared to scattering or fluorescent imaging.

As a consequence, the accuracy of the particle z location determination is smaller for the shadow-

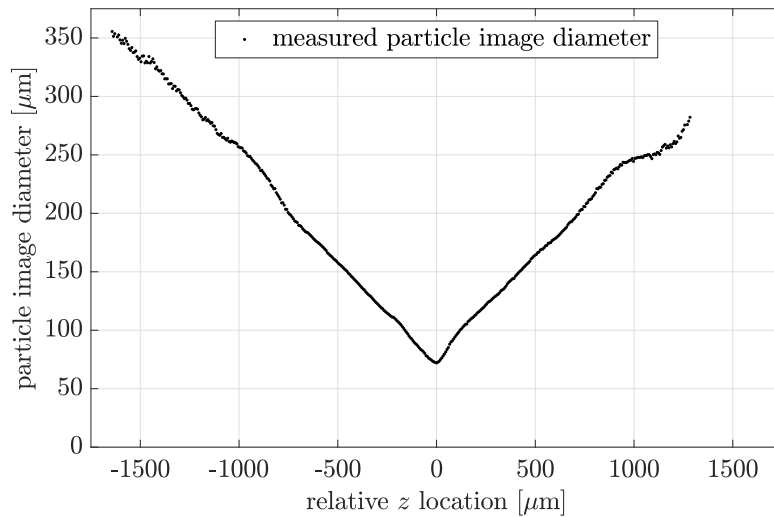


Figure 4. Defocusing function with the focal plane at $z = 0 \mu\text{m}$. The linear slope of the function on each side of the focal plane yields $s^Z \approx 0.18$, meaning that for given change of the particle location Δz , the particle shadow image diameter changes by a 0.18 of this value. The particle was scanned through the domain in steps of $5 \mu\text{m}$.

graph imaging configuration. However, shadowgraphy enables to extend the measurement depth significantly, since the SNR of the particle images is still large enough to determine their diameter even at a distance of almost $1500 \mu\text{m}$ away from the focal plane. Moreover, the particle image densities can be much higher, due to their smaller diameters. Figure 4 also reveals that the defocusing function is nearly symmetrical with respect to the focal plane. This does not only apply for s^Z , but this also applies for the appearance of the particle images, since it cannot be distinguished on which side of the focal plane the corresponding particles are situated. As outlined by Rossi (2019), this symmetry is not a typical observation when using scattered light imaging or fluorescence in microscopic imaging systems, where the particle images show distinct differences depending on which side of the focal plane the particles are located.

Furthermore, it becomes evident that the defocusing function is not exactly linear for the defocusing shadowgraphy set-up (see Fig. 4). At the focal plane, the slope is zero, and then it increases, reaching a range where it close to being linear, around $150\text{--}600 \mu\text{m}$ away from focal plane. After that, the detection of the particle shadow images becomes more and more difficult, since the SNR decreases, emphasized by the increased scatter of the diameter values. Unfortunately, the non-linear behaviour of the defocusing function leads to the fact that it is not feasible to perform an *in situ* calibration, since this relies on a linear change of the particle image diameter with respect to the particle z location. Hence, this defocusing shadowgraphy approach requires a scanning calibration, just as it is the case for other microscopic defocusing and astigmatism particle imaging methods. In the following, it is described how introducing astigmatism to the optical path helps to improve this defocusing set-up.

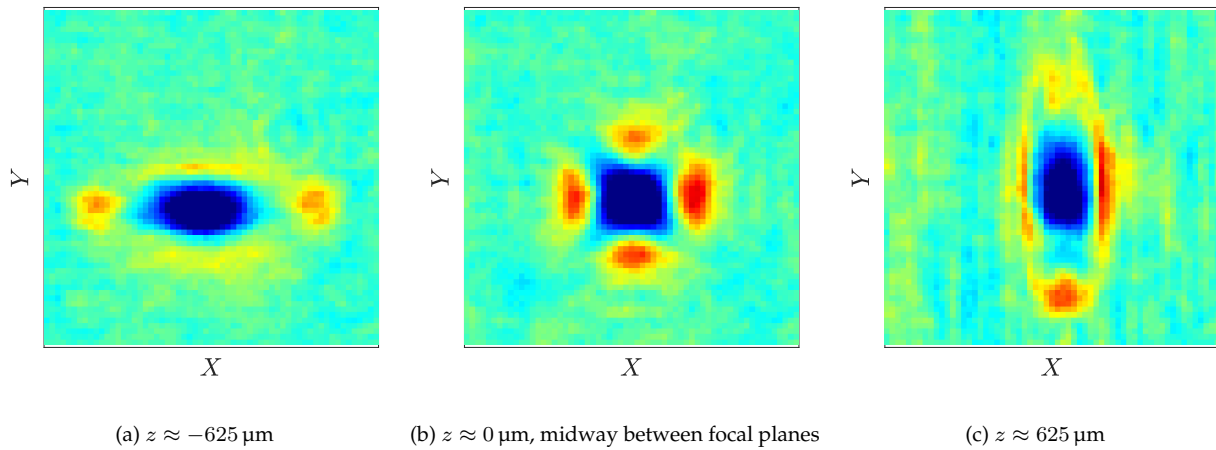


Figure 5. Particle shadow images forming in the presence of astigmatism in the optical system. The images form ellipses, except for the plane of least distortion, at $z = 0$, midway between the two focal planes, where the axis lengths in sensor X and Y direction are equal.

3. Astigmatism shadowgraphy

Astigmatic particle shadow image characteristics

In astigmatic imaging set-ups the optical symmetry with respect to focal plane is broken, for instance, by placing a cylindrical lens on the optical light path. As a result, a second focal plane emerges that is oriented perpendicular to the other focal plane, such that the particle images form ellipses. As it was outlined by Cierpka & Kähler (2012), the advantage of the astigmatic optics is that the measurement depth is increased, due to the fact that the region with sufficient SNR also increases. In addition, the SNR value is distributed more homogeneously along the measurement depth.

Examples of astigmatic particle shadow images are shown in Fig. 5. On the left ((Fig. 5(a)) at $z \approx -625 \mu\text{m}$ relative to the plane of least distortion (located midway between the focal planes, at $z = 0 \mu\text{m}$), the particle shadow image forms an ellipse, where the major axis extends along the X sensor coordinate. The shadow image center has an intensity that is lower than the background intensity. At the vertices of the ellipse, distinct intensity peaks form, while they show a larger intensity at the left and the right vertex than compared to the upper and lower vertex. Midway between the focal planes (Fig. 5(b)), the particle shadow image has a symmetric shape, again with an intensity valley in the center. The intensity peaks at the four ellipse vertices appear similar. At $z \approx 625 \mu\text{m}$ (Fig. 5(c)), the shadow image looks like its counterpart at $z \approx -625 \mu\text{m}$, only that the orientation turned by 90° , such that the major axis is oriented along the sensor Y coordinate.

The astigmatic configuration is equal to the defocusing configuration, shown schematically in Fig. 1, except for the fact that a cylindrical lens with a focal length of 150 mm was placed between the microscope objective and the measurement domain. Furthermore, all other processing steps and imaging procedures are equivalent to that of the defocusing approach.

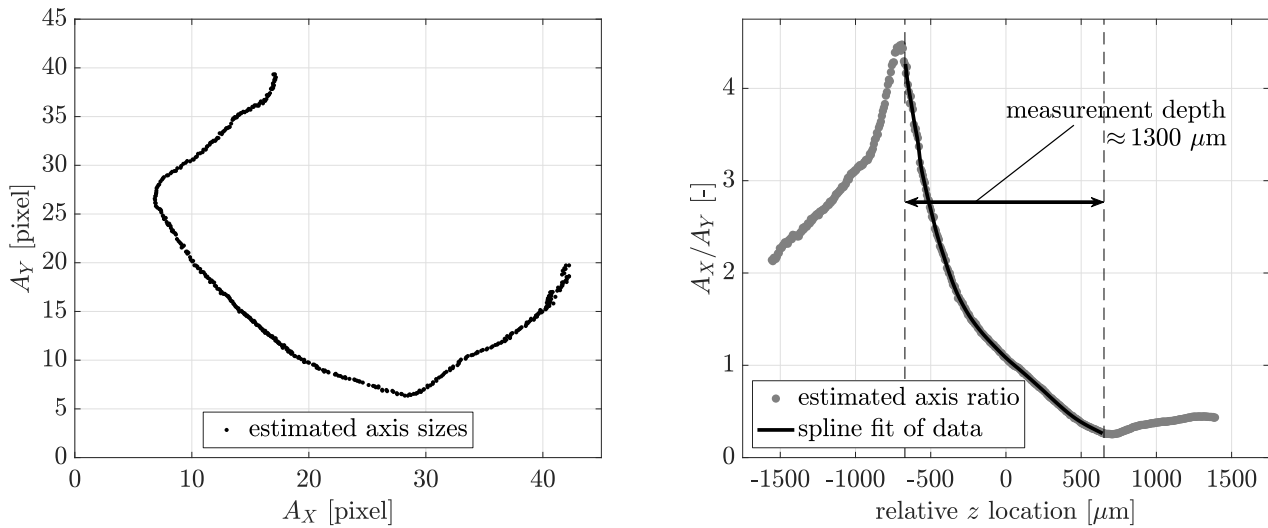
(a) The relation between the axis length in sensor X and Y direction.(b) The axis lengths ratio A_X/A_Y as a function of z .

Figure 6. Functional relations of the axis lengths in sensor X and Y direction as a function of z . The particle was scanned through the domain in steps of $5 \mu\text{m}$.

Astigmatic characteristics

Unlike for defocusing imaging, where the diameter is sufficient for describing the particle image geometry, the elliptically shaped particle images in astigmatic imaging use the extent/axes length of the ellipse, A_X and A_Y , in sensor X and Y direction. For the optical set-up used in this study, the relation between A_X and A_Y is plotted in Fig. 6(a), where the minimum of each axis length denotes the location of the corresponding focal plane. It is a common approach in astigmatic imaging to determine the minimal euclidean distance to this relation to derive the particle z location from the particle axis length (Cierpka et al. (2010), Brockmann & Hussong (2021)). The latter approach helps to determine particle locations beyond the focal plane locations, i.e. their absolute distance to the plane of least distortion is larger than the focal plane distance to this reference plane. However, close to the focal planes, the uncertainty of the particle is relatively large, due to small rate of change of the axis lengths over z , such that it is beneficial to measure between the focal planes only. Due the smaller s^Z value of the shadowgraphy approach, the distance between the focal planes can be chosen large enough to measure between the focal planes only. As suggested by Fuchs et al. (2014), it is then feasible to use the axis ratio, A_X/A_Y , as a single parameter to describe the elliptical particle shadow images. Figure 6(b) shows A_X/A_Y as a function of z , where the solid black line denotes the calibration function, which was determined by a spline fit of the measurement data. For the present set-up, the measurement depth of the astigmatic shadowgraphy configuration yields around $1300 \mu\text{m}$, which is sufficient for conducting measurements in the microscopic range and beyond. Thus, the presented approach is capable of measuring over a large length scale range, making it a versatile tool for a variety of applications. Moreover, the focal plane distance and therefore the measurement depth can be increased by placing a cylindrical lens with a smaller focal length between the objective lens and the measurement domain.

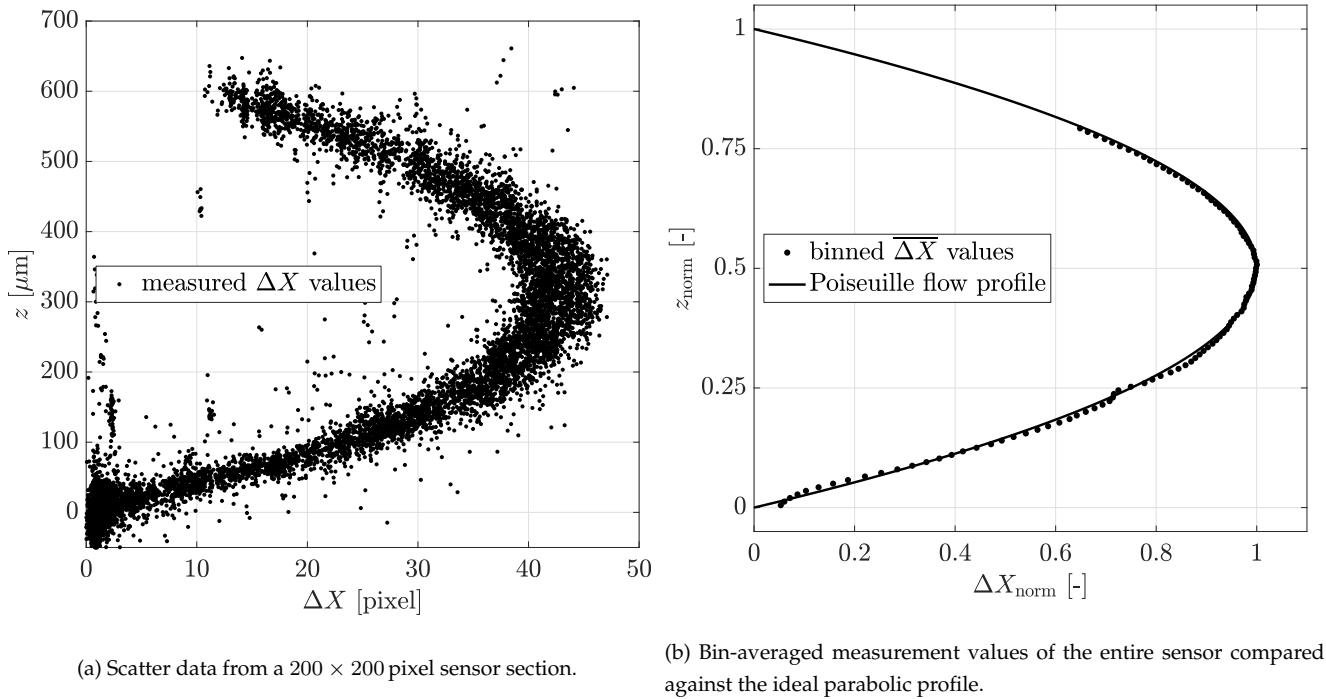


Figure 7. Measurement data, ΔX over z , for a micro-channel (channel height: $650 \mu\text{m}$) flow. A time-series of 2500 images was recorded at a frequency of 0.1 kHz and a camera exposure time of $30 \mu\text{s}$ for the shown data.

Micro-channel flow

As a means to prove the feasibility of this particle shadow imaging PTV approach, a Poiseuille-flow was measured in a micro-channel with $h \approx 650 \mu\text{m}$ channel height, a width of 5 mm and a length of 50 mm. A time-series of 2500 images were recorded at frequency of 0.1 kHz. Figure 7(a) shows the measurement values, ΔX over z , in a 200×200 pixel sensor section after a nearest-neighbour tracking procedure without further post-processing. Close to the upper channel wall, there are no measurement values due to the settled particles. The number of spurious data points is relatively low, such that suitable outlier detection methods are able to detect these data points. Comparing the normalized bin averaged ΔX_{norm} values (black markers) of the entire measurement data to the ideal parabolic profile of the Poiseuille-flow (solid black line) in Fig. 7(b) yields a good agreement, giving rise to the assumption of the validity of these initial measurements. However, a more thorough uncertainty analysis is required to assess the capabilities of this defocusing shadowgraphy method.

4. Conclusion

Shadowgraph imaging provides a viable means to avoid the use of fluorescence in microscopic particle imaging. The particle shadow image geometry can be employed to determine the particle location along the optical axis, enabling a 3D flow measurement in microscopic domains. However,

the defocusing characteristics of shadowgraph imaging, using an almost parallel background illumination, are significantly different as compared to the characteristics of fluorescence/scattering imaging set-ups. Mainly, the rate of the particle shadow image diameter change with distance from the focal plane is significantly smaller than compared to fluorescence/scattering particle images. As a result, larger measurement depths can be achieved, since the SNR of the relatively small particle shadow images is still large enough for detection, even at distances of more than 1000 μm from the focal plane at a magnification of $M = 6.2$. Moreover, due to the smaller particle shadow image dimensions, making overlaps less likely, the number of particles that can be imaged simultaneously is relatively high, such that in a single recording around 350 particles were captured on a 2000×2000 pixel sensor.

Introducing astigmatism to the shadowgraphy system yields an even increased measurement depth, since the limitation of being able to measure on only one side of the focal plane in a defocusing configuration is overcome. The feasibility to use shadowgraphy for microscopic PTV was proven by means of a micro-channel (channel height: 650 μm) flow measurement, where the velocity values showed a good agreement with the ideal parabolic profile of the Poiseuille flow. Altogether, shadowgraphy nicely complements the microscopic particle imaging methods based on fluorescence by extending the range of applications to larger measurement depths as well as to investigations where the use of surfactants influences the results.

References

- Barnkob, R., Kähler, C. J., & Rossi, M. (2015). General defocusing particle tracking. *Lab on a Chip*, 17, 3556–3560. doi: 10.1039/c5lc00562k
- Brockmann, P., & Hussong, J. (2021). On the calibration of Astigmatism particle tracking velocimetry for suspensions of different volume fractions. *Experiments in Fluids*, 62(1), 23. doi: 10.1007/s00348-020-03120-4
- Cierpka, C., & Kähler, C. J. (2012). Particle imaging techniques for volumetric three-component (3D3C) velocity measurements in microfluidics. *Journal of Visualization*, 15(1), 1–31. doi: 10.1007/s12650-011-0107-9
- Cierpka, C., Rossi, M., Segura, R., & Kähler, C. J. (2010). On the calibration of astigmatism particle tracking velocimetry for microflows. *Measurement Science and Technology*, 22(1), 15401. doi: 10.1088/0957-0233/22/1/015401
- Fuchs, T., Hain, R., & Kähler, C. J. (2014). Three-dimensional location of micrometer-sized particles in macroscopic domains using astigmatic aberrations. *Optics Letters*, 39(5), 1298–1301. doi: 10.1364/OL.39.001298

- Fuchs, T., Hain, R., & Kähler, C. J. (2016). In situ calibrated defocusing PTV for wall-bounded measurement volumes. *Measurement Science and Technology*, 27(8), 084005. doi: 10.1088/0957-0233/27/8/084005
- Kao, H. P., & Verkman, A. S. (1994). Tracking of single fluorescent particles in three dimensions: use of cylindrical optics to encode particle position. *Biophysical Journal*, 67(3), 1291–1300. doi: 10.1016/S0006-3495(94)80601-0
- Leister, R., Fuchs, T., Mattern, P., & Kriegseis, J. (2021). Flow-structure identification in a radially grooved open wet clutch by means of defocusing particle tracking velocimetry. *Experiments in Fluids*, 62(2), 29. doi: 10.1007/s00348-020-03116-0
- Olsen, M. G., & Adrian, R. J. (2000). Out-of-focus effects on particle image visibility and correlation in microscopic particle image velocimetry. *Experiments in Fluids*, 29(1), S166—S174. doi: 10.1007/s003480070018
- Rossi, M. (2019). Synthetic image generator for defocusing and astigmatic PIV/PTV. *Measurement Science and Technology*, 31(1), 17003. doi: 10.1088/1361-6501/ab42bb
- Rossi, M., & Kähler, C. J. (2014). Optimization of astigmatic particle tracking velocimeters. *Experiments in Fluids*, 55(9), 1809. doi: 10.1007/s00348-014-1809-2
- Thijssen, J. H. J., Schofield, A. B., & Clegg, P. S. (2011). How do (fluorescent) surfactants affect particle-stabilized emulsions? *Soft Matter*, 7(18), 7965–7968. doi: 10.1039/C1SM05968H
- Willert, C., & Gharib, M. (1992). Three-dimensional particle imaging with a single camera. *Experiments in Fluids*, 12(6), 353–358. doi: 10.1007/BF00193880